In-situ SERS monitoring of reaction catalyzed by multifunctional Fe₃O₄@TiO₂@Ag-Au microspheres

Jianhua Shen [a,1], Ying Zhou [a,1], Jianfei Huang [a], Yihua Zhu [a,*], Jingrun Zhu [a], Xiaoling Yang [a], Wei Chen [a], Yifan Yao [a], Shaohong Qian [b], Hao Jiang [a], Chunzhong Li [a,*]

[a] *Key Laboratory for Ultrafine Materials of Ministry of Education, School of Materials Science and Engineering, East China University of Science and Technology, Shanghai 200237, China*
[b] *Department of Ophthalmology, EENT Hospital of Fudan University, 83 Fenyang Road, Xuhui District, Shanghai 200031, China*

ABSTRACT

Multifunctional Fe₃O₄@TiO₂@Ag-Au microspheres (MS) were synthesized by grafting Ag nanoparticles onto 3-Aminopropyltrimethoxysilane (APTMS) modified Fe₃O₄@TiO₂ MS, followed by galvanic replacement approach to fabricate Ag-Au bimetallic nanostructures with variable bimetallic molar ratios. The composite with Au-to-Ag ratio of 1:1 exhibits optimal catalytic activity for reduction of 4-nitrophenol (4-NP). Furthermore, finite-difference time-domain (FDTD) simulation study shows that incorporating Au-Ag bimetallic nanostructures onto Fe₃O₄@TiO₂ MS significantly increases the effect of the 'hot spot', offering stronger electromagnetic field enhancements. Indeed, the Fe₃O₄@TiO₂@Ag-Au was demonstrated to be an excellent substrate material for in-situ surface-enhanced Raman scattering (SERS) monitoring of the reaction process. Combined with its good magnetic and photocatalytic performance allowing facile recovery, Fe₃O₄@TiO₂@Ag-Au MS shows great potential for multifunctional platform for simultaneous catalysis and in-situ reaction monitoring.

© 2016 Elsevier B.V. All rights reserved.

1. Introduction

Noble metal nanoparticles (NPs) have arose more and more regard due to their inimitable physicochemical properties, leading to widespread applications in the fields of catalysis, electrochemistry, sensors and biomedicine [1–3]. Over the past few decade, Au NPs have oriented heterogeneous catalysis, displaying distinctive properties in terms of both excellent selectivity and high activity for many chemical reactions [4]. Moreover, their high surface energy with sizes in the low nanometer range usually results to aggregation and decrease their catalytic activity [5–8]. Furthermore, various nanosized bimetals with core-shell, heterostructured, or alloy architectures captured much attention due to the electronic properties originated from the intrinsic nature of two different metals [9,10]. Particularly for heterogeneous catalysis, bimetallic nanomaterials exhibit unprecedentedly enhanced catalytic capability compared with monometallic nanocrystals [11].

UV–vis spectroscopy is a simple and reliable technique frequently applied to investigate catalytic activity and reaction kinetics [12–15]. However, it offers limited information, and thus limited access to tracking the reaction process. In comparison, surface-enhanced Raman spectroscopy (SERS) possesses high chemical specificity, sensitivity, and surface selectivity [16–18]. In spite of much progress has been made in the label-free in-situ monitoring of heterogeneous catalysis, even now, it is a challenge to prepare bimetallic nanostructures with both good catalytic activity and high SERS activity. Bimetallic NPs often show better SERS activity and catalytic performance compared with their corresponding monometallic counterparts [19]. Usually, the combination of Au with metals such as Pt or Pd provides an occasion for label-free in-situ monitoring of Pt or Pd catalysed reactions by SERS. However, difficulties exist in Raman spectroscopy of molecules adsorbed on Pt or Pd, where intense suppression of plasmon resonances of Au were resulted [20]. Only a few bimetallic nanostructures can meet the demands as the SERS-active substrates for in-situ monitoring, because the SERS-active surface is mainly limited to Au, Ag and Cu [21]. Efficient substrate materials for in-situ SERS for monitoring catalytic reactions requests for: (1) simultaneously possessing catalytic activity and strong local surface plasmonic resonance effect, (2) adaptability to simple immobilization on substrate and (3) the recoverability of catalysts and substrates to reduce the cost. Accordingly, some attempts were made. For instance, Xie et al. prepared

bifunctional Au/Pt/Au nanoraspberries for in-situ monitoring of Pt-catalysed reactions by SERS [22]. And they also demonstrated 3D plasmonic superstructures of Au NPs for label-free SERS monitoring of catalytic reactions [23]. Moreover, Cao et al. prepared bifunctional polyacrylonitrile/Ag-M nanofibers as substrates for SERS monitoring catalytic reactions [24]. Joseph et al. immobilized separate Au and Pt NPs on the glass substrate surface to monitor the catalytic reactions by SERS [25]. While inspiring, these efforts still cannot fully satisfy all the requirements mentioned above.

Magnetic nanomaterials are of great interest in many fields due to their rapid magnetic response under an applied magnetic field. The superparamagnetic natures endow their efficient separation of catalysts from the reaction system [26]. Particularly, the composites of magnetic iron oxide with noble metal NPs results in concurrent magnetic and optical responses. Specifically, for SERS, external field-directed self-arrangement of substrate materials may contribute to the enhanced SERS activity, as demonstrated previously reported Ag-coated Fe_3O_4 composites [27] as the surfactant-free SERS substrate and multifunctional Fe_3O_4/C/Au NPs [28] for high sensitive in-situ monitoring of catalytic reactions. Another problem plaguing efficient utilization of reuse of catalysts originates from difficulty in removing the absorbed organic chemicals from the catalysed synthesis system. In this context, photocatalytically active material such as TiO_2 can be introduced to destroy these molecules in order to reactivate catalysts [29]. Integration of Au-Ag and TiO_2 can also improve the photocatalytic capability of TiO_2 under visible light, promoting self-cleaning performance.

Herein, we report the synthesis of magnetic and recyclable multifunctional composite with Fe_3O_4 inner core, TiO_2 interlayer and Ag-Au bimetallic nanostructures, designated $Fe_3O_4@TiO_2@Ag$-Au (as shown in Scheme 1a), which was obtained by uniform coating Fe_3O_4 microspheres (MS) with TiO_2 through sol-gel process and modification of $Fe_3O_4@TiO_2$ MS with 3-Aminopropyltrimethoxysilane (APTMS), followed by coating with a layer of Ag NPs and subsequent galvanic replacement to grow bimetallic Ag-Au nanostructure. The catalytic activity of the composite was tested by with the reduction of 4-Nitrophenol (4-NP) to 4-Aminophenol (4-AP) as the model reaction (Scheme 1b). Further, the reduction of 4-Nitrothiophenol (4-NTP) to 4-Aminothiophenol (4-ATP) was chosen for studying the functionality of in-situ SERS monitoring (Scheme 1c).

2. Experimental

2.1. Synthesis of $Fe_3O_4@TiO_2@Ag$-Au MS

The preparation of $Fe_3O_4@TiO_2@Ag$ MS had been reported in our past work, and the detailed experimental procedures are displayed in the Supplementary data. 10 mL of 0.1 M Benzyldimethylhexadecylammonium chloride (BDAC), 421 μL of 0.01 M $HAuCl_4$, 512 μL of 0.01 M $AgNO_3$ and 268 μL of 0.1 M ascorbic acid were mixed sequentially at 30 °C in a 20 mL glass vial. After 5 min, different volume of as-prepared of $Fe_3O_4@TiO_2@Ag$ solution ranging from 0.25 mL, 0.5 mL to 1.0 mL was added into 50 mL of growth solution with stirring (10 s). Then the solution was left undisturbed for 1 h at 30 °C. Samples were then separated and collected using external magnetic field and washed with ultrapure water and ethanol for 3 times respectively to remove excess amounts of surfactants. The precipitates were redispersed in water for characterization. The more characterizations are also shown in the Supplementary data.

2.2. Finite-difference time-domain (FDTD) calculations

The distribution of electromagnetic field intensity around the $Fe_3O_4@TiO_2@Ag$-Au MS and $Fe_3O_4@TiO_2@Ag$ MS was calculated

using the FDTD method. The FDTD Solutions software package (Lumerical Solutions Inc., Vancouver Canada) was used to carry out the computational calculations and numerical analysis. The mesh size was 1 nm. The calculation time was 1000 fs.

3. Results and discussion

3.1. Synthesis and characterization of the fourfold $Fe_3O_4@TiO_2@Ag$-Au core-shell MS

As shown in Scheme 1a, the fourfold $Fe_3O_4@TiO_2@Ag$-Au core-shell MS was composed of Fe_3O_4 core, TiO_2 interlayer, and the outer layer of Ag-Au bimetallic nanostructure. The well-defined Fe_3O_4 MS were first synthesized through a robust solvothermal reaction based on the high reduction of Fe^{3+} with ethylene glycol [30], the magnetic core ensures the convenient separation of the catalysts from the reaction system as well as the controllable arrangement of bimetallic SERS substrate. The uniform gray TiO_2 interlayer with a thickness provides a continuous coverage of Fe_3O_4 [31], which facilitates not only the absorption of reactants but also the degradation of organics so that the composites can be reused. And then, the prepared $Fe_3O_4@TiO_2$ core-shell MS are modified by APTMS to afford their surfaces with amino groups. Finally, the modified $Fe_3O_4@TiO_2$ core-shell MS were mixed with as-prepared Ag NPs to make a graft of Ag NPs onto the surfaces of $Fe_3O_4@TiO_2$ MS [32], then accompanied with controllable galvanic replacement approach to fabricate bimetallic nanostructure of Ag-Au with variable morphology.

SEM image reveals that the magnetic Fe_3O_4 MS have an average diameter of ~200 nm (Fig. 1a). The uniform layer of TiO_2 with the thickness of ~20 nm provides the continuous coverage of Fe_3O_4 cores (Fig. 1b). The obtained $Fe_3O_4@TiO_2$ core-shell MS are modified by APTMS to render the surfaces with amino groups. The modified $Fe_3O_4@TiO_2$ MS were grafted with Ag NPs through the strong chemical bonding between amine groups and Ag NPs. As shown in TEM image (Fig. 1c), Ag NPs with the diameter of ~5 nm were well-dispersed on $Fe_3O_4@TiO_2$ MS with no obvious aggregation. Ag-Au bimetallic structures supported on $Fe_3O_4@TiO_2$ composites were synthesized with the $Fe_3O_4@TiO_2@Ag$ serving as starting material, which were served as reductant for galvanic replacement reaction. By varying the amount of $Fe_3O_4@TiO_2@Ag$, the compositions of Ag-Au bimetallic structure on $Fe_3O_4@TiO_2$ MS could be readily controlled, resulting in spiny surfaces of the prepared composites with different Au-to-Ag molar ratios ranging among 1:2, 1:1, 2:1, as shown in the SEM (Fig. 1d–f) and TEM (Fig. 1g–i) images. SEM images revealed that the petals of flowerlike structure become more obvious with increasing Au-to-Ag molar ratios, and TEM images showed the inner structure of the composites. When the Au-to-Ag molar ratios is 1:1, more voids existed within the Au-Ag nanostructured dendrite layers, which can serve to promote the interaction between reactant molecules and catalyst, and provide more nanosized gaps for effect of SERS. From the SEM and TEM images, $Fe_3O_4@TiO_2@Ag$-Au (1:1) MS possess the rough surface and porous. As shown in Fig. S1, the type-IV isotherm with a type-H3 hysteresis loop is displayed, which is indicated the mesoporous structure. The inset describes two relatively narrow pores (ca. 3.7 and 16.4 nm) in the size distributions using the Barrett-Joyner-Halenda (BJH) method, which indicates the presence of textural mesopores in the Ag-Au shells. Such a porous structure gives rise to the high specific surface area of 77.7 $m^2 g^{-1}$.

Wide-angle X-ray diffraction (XRD) patterns of Fe_3O_4 MS (black), $Fe_3O_4@TiO_2$ MS (blue), $Fe_3O_4@TiO_2@Ag$ MS (green) and $Fe_3O_4@TiO_2@Ag$-Au MS (red) during different stages are shown in Fig. 2. The characteristic broad diffraction peaks in XRD patterns can be indexed to Fe_3O_4, anatase TiO_2 and alloyed phase Ag-Au in the composite MS, respectively. The six peaks at 2θ values of 30.0, 35.3,
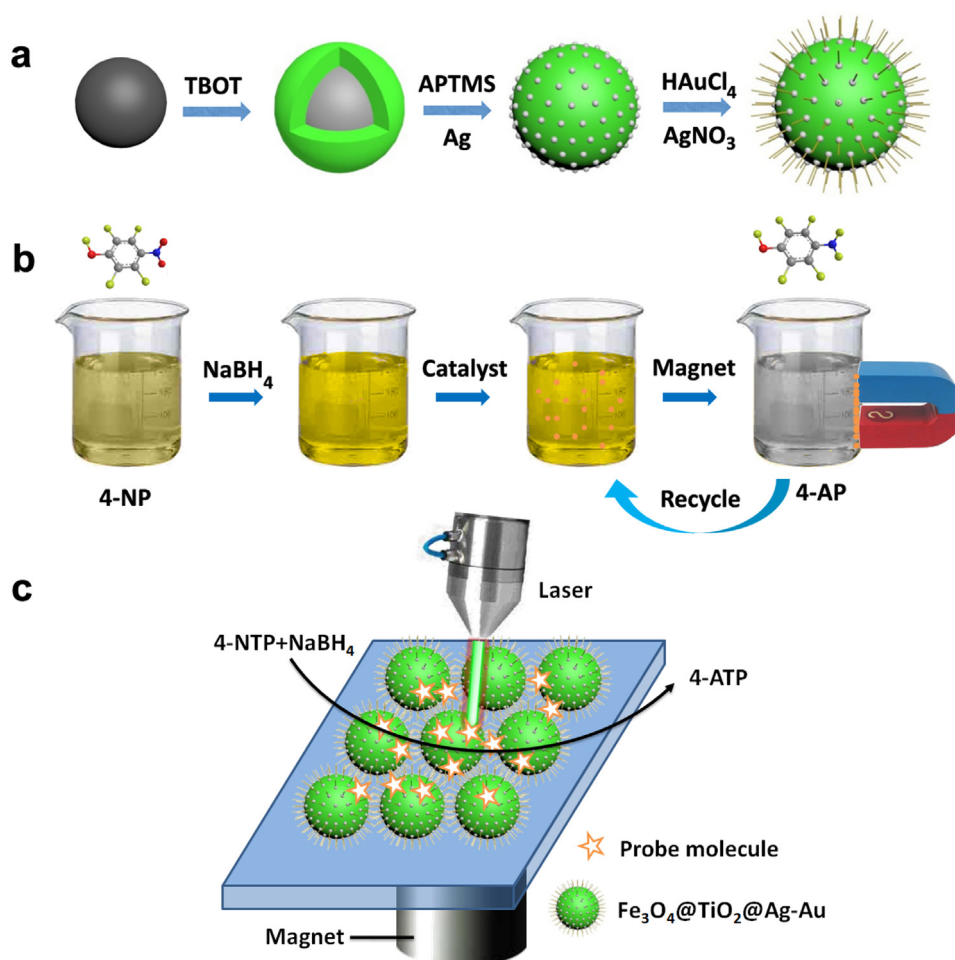
Scheme 1. Schematic diagrams for (a) the preparation of Fe$_3$O$_4$@TiO$_2$@Ag-Au MS, (b) the catalytic reduction of 4-NP with Fe$_3$O$_4$@TiO$_2$@Ag-Au MSs in the presence of NaBH$_4$ and (c) in-situ monitoring of the reduction reaction.

42.9, 53.5, 57.0 and 62.4° are corresponding to [220], [311], [400], [422], [511] and [440] planes of the cubic phase of Fe$_3$O$_4$ (JCPDS card No. 01-075-0449), respectively. After the coating of TiO$_2$ layers and subsequent hydrothermal treatment, the pattern for the Fe$_3$O$_4$@TiO$_2$ additionally shows several peaks, which is attributed to the anatase phase of TiO$_2$ (JCPDS card No.01-075-2545). The peaks corresponding to the [101], [004], [200], and [105] planes of the anatase phase contribute to some additional peaks located at 25.3, 37.9, 48.0 and 53.9°. Loading Ag NPs and Au-Ag dendrites on the surface of Fe$_3$O$_4$@TiO$_2$ MS, additional diffraction peaks from the [111], [200] and [220] crystal planes pure Ag and pure Au phase.

The magnetic hysteresis loops of the bare Fe$_3$O$_4$, Fe$_3$O$_4$@TiO$_2$, Fe$_3$O$_4$@TiO$_2$@Ag and Fe$_3$O$_4$@TiO$_2$@Ag-Au MS at room temperature are shown in Fig. S2. All of them display superparamagnetic behavior and little hysteresis, remanence and coereivity due to the fact that the particles are composed of ultrafine magnetite nanocrystals. As shown, the magnetic saturation value of Fe$_3$O$_4$ MS is about 53.2 emu/g, and that of Fe$_3$O$_4$@TiO$_2$, Fe$_3$O$_4$@TiO$_2$@Ag and Fe$_3$O$_4$@TiO$_2$@Ag-Au MS are about 41.1, 33.6 and 26.1 emu/g, respectively. By contrast, decrease in magnetization is mainly ascribed to the decrease in the proportion of Fe$_3$O$_4$ in the prepared composites after coating with TiO$_2$ and Ag-Au. But it should be noted that Fe$_3$O$_4$@TiO$_2$@Ag-Au still displayed strong magnetization, which suggested their applicability for magnetic separation and rearrangement of SERS substrate. Under the external magnetic field, these composites were immediately attracted to one side of

the vial with several seconds and the solution turned into transparent.

3.2. Application of the Fe$_3$O$_4$@TiO$_2$@Ag-Au MS for the catalytic reduction of 4-NP

Bimetallic structures were evidenced to be outstanding catalysts owing to the synergistic effect of the two different noble metals. The catalytic reduction reaction of 4-NP to 4-AP in the presence of NaBH$_4$ was selected as the model reaction to study the catalytic activity of Fe$_3$O$_4$@TiO$_2$@Ag-Au MS [33]. The original 4-NP solution is light yellow and displays the obvious spectral profile with the maximal absorbance at 317 nm in Fig. S3, upon the addition of NaBH$_4$, the absorbance peaks shift to 400 nm, corresponding to the color change from light yellow to bright yellow for the existence of 4-NP ion in alkaline condition is observed immediately [34,35]. And there is no change in the absorbance at 400 nm over time, revealing the reduction is difficult to proceed without a catalyst.

UV-vis spectra monitoring the reduction reactions of 4-NP, measured at different times using Fe$_3$O$_4$@TiO$_2$@Ag-Au MS of different Au/Ag molar ratios (0:1, 1:1, 1:2, 2:1) as catalysts are shown in Fig. 3. Take the case of 1:2 for example, the 400 nm absorption peak steadily decreased in intensity as the reaction proceed for 20 min; meantime the new peak at 300 nm emerged and increased in intensity, which was attributed to the 4-AP absorption, the corresponding daughter derivatives of 4-NP. Similarly, the same amount of catalysts with different Au/Ag molar ratio were added as cata-
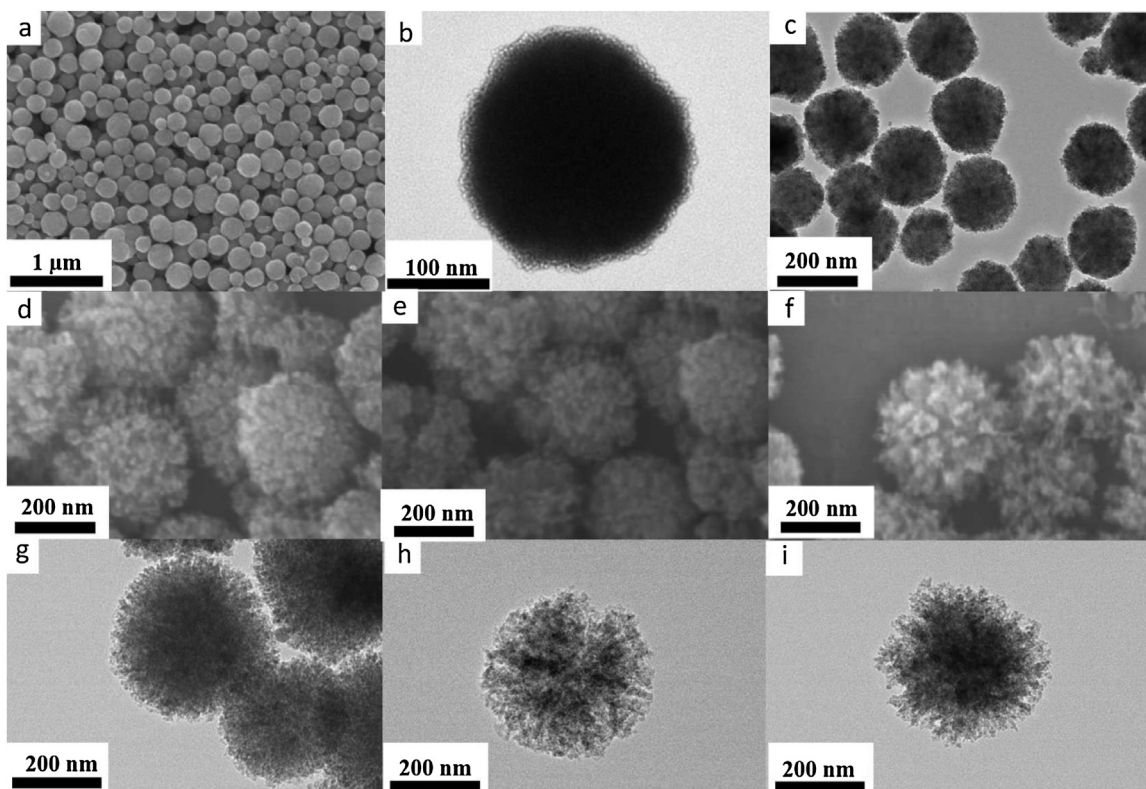
Fig. 1. (a) SEM image of Fe_3O_4 MS. (b) TEM image of $Fe_3O_4@TiO_2$ core-shell MS with a uniform TiO_2 shell thickness of 35 nm. (c) SEM image of $Fe_3O_4@TiO_2@Ag$ (5 nm). (d-f) SEM image of $Fe_3O_4@TiO_2@Ag$-Au with various molar ratio of Au/Ag ranging from 1:2, 1:1 to 2:1 and (g-i) the corresponding TEM images.
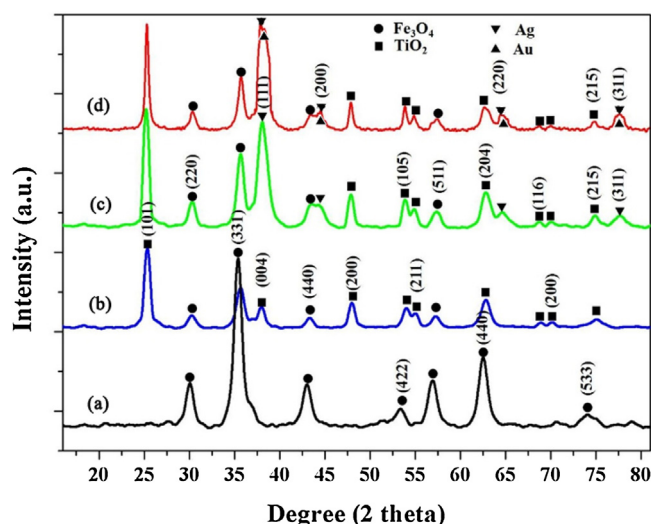
**Fig. 2.** XRD patterns of (a) Fe_3O_4, (b) $Fe_3O_4@TiO_2$, (c) $Fe_3O_4@TiO_2@Ag$ and (d) $Fe_3O_4@TiO_2@Ag$-Au Ms.

lysts, the adsorption peak at 400 nm decreased in intensity after 30 min for 0:1 ($Fe_3O_4@TiO_2@Ag$), 12 min for $Fe_3O_4@TiO_2@Ag$-Au (1:1) and 16 min for $Fe_3O_4@TiO_2@Ag$-Au (2:1), and the peak at 300 nm increased accordingly (Fig. 3). And as shown in Fig. S4, the reaction time of the control sample $Fe_3O_4@TiO_2@Au$ is about 21 min.

As shown Eq1 in the Supplementary data, the linear relationships between $\ln(C_t/C_0)$ and the reaction time t are shown in Fig. 3, which match well with the first-order reaction kinetics [36–38]. Insets in Fig. 3 express the variable κ values, where the nature of the bimetallic nanostructures in the composites

was tuned by exactly controlling the Au/Ag molar ratios (0:1, 1:2, 1:1, 2:1). $Fe_3O_4@TiO_2@Ag$ MS (0:1) were also investigated as the control; they displayed comparatively poor catalytic property, with the lowest activity index (κ = 315.07 s^{-1} g^{-1}). And the $Fe_3O_4@TiO_2@Au$ sample without Ag NPs possessed the activity index (κ = 447.80 s^{-1} g^{-1}). When the bimetallic structure was formed on $Fe_3O_4@TiO_2$ MS, catalytic capability of samples was facilitated. With the variable ratio, κ correspondingly varied, achieving values as high as 548.05 s^{-1} g^{-1}, 1564.9 s^{-1} g^{-1} and 2433.17 s^{-1} g^{-1} for case of Au/Ag ratio of 1:2, 2:1, and 1:1, much higher than the previously reported Ag or Au monometallic composites [39–41]. The outstanding catalytic performance of $Fe_3O_4@TiO_2@Ag$-Au can be attributed to the nature of bimetallic nanocrystal supported on $Fe_3O_4@TiO_2$, these bimetallic structure provides an intimate contact between Ag and Au and permits for an electronic communication which can actuate the reaction [42]. Despite the ionization potentials of Au and Ag are 9.22 and 7.58 eV [43], it would have occurred that electron transfer from Ag to Au leading to exposure of electron-rich catalytically active sites which promote BH^{4-} to capture the nitro group of the 4-NP molecule. All of these factors promoted catalytic capabilities of the catalysts pronouncedly. As reported, higher catalytic ability can be obtained upon Au-rich samples for the reason that Au has higher rate constant for such reduction than Ag [44]. In this work, the rate constant did not increase with increasing proportion of Au in composites, it is supposed that the catalytic activity of the Ag-Au nanocrystals was influenced by both Au concentrations in the bimetallic nanoparticles and structure of composites. When the Au/Ag ratio is 1:1, TEM images display much voids exist inside which could serve as nanoreactors beneficial for the close contact between reactant molecules and catalysts, the common efforts of appropriate Auto-Ag molecular ratio and structural advantages contribute to the excellent catalytic performance.
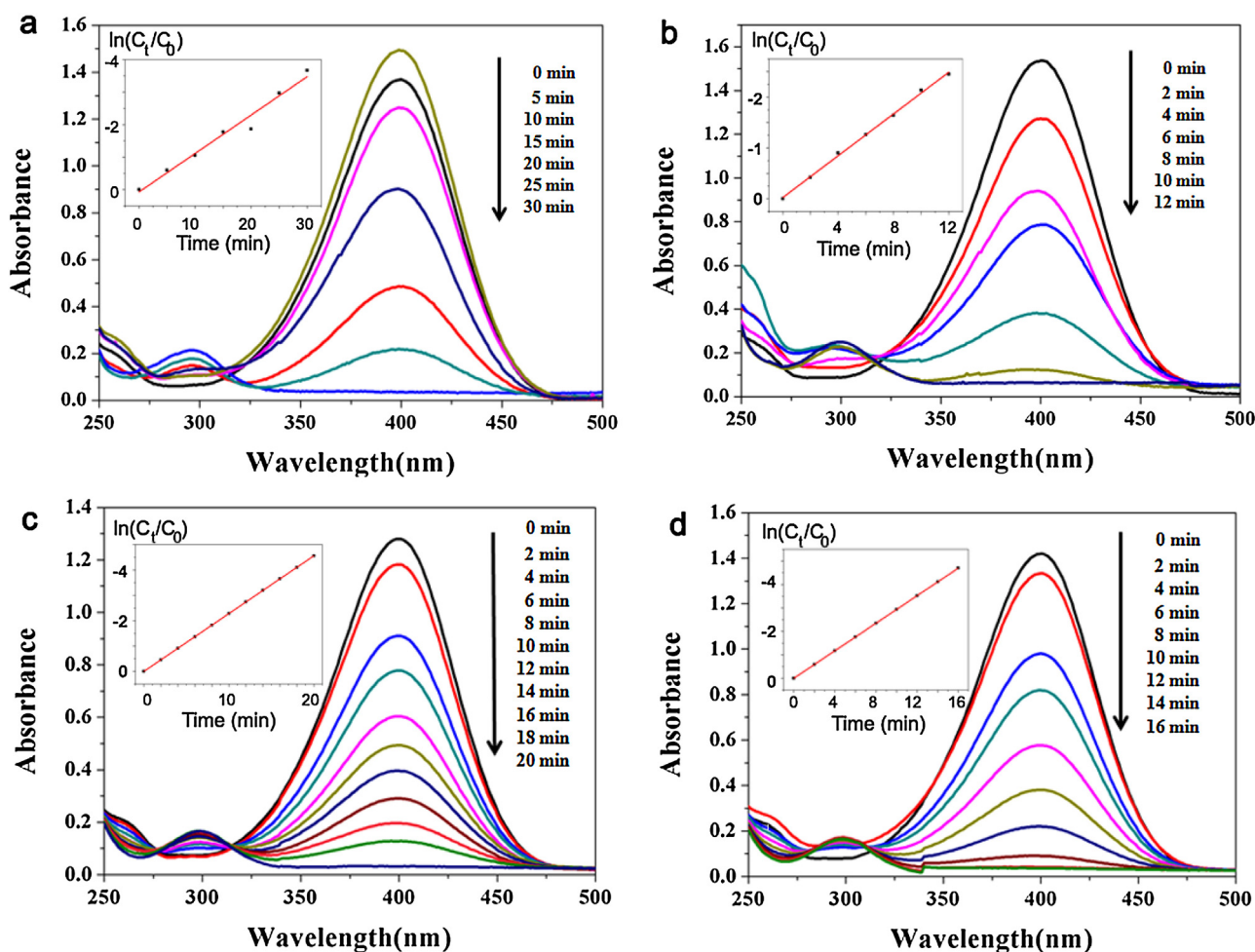
Fig. 3. Catalytic reduction of 4-NP conducted with different catalysts: $Fe_3O_4@TiO_2@Ag$-Au with various molar ratio of Au/Ag ranging from 0:1, 1:1, 1:2 to 2:1, the inset pattern is the relationship of the $\ln(C_t/C_0)$ versus the reaction time for the reduction of 4-NP over $Fe_3O_4@TiO_2@Ag$-Au MS of different ratios respectively at 25 °C. C_0 and C_t is the absorption peak at 400 nm initially and at time t.

As we all known, the LSPR is one of distinctive features of Au and Ag nanoparticles. Under the visible light, the strong electromagnetic field enhancements can also increase their catalytic activities [45]. As shown in Fig. S5, the activity index κ (Fig. S5 black line) was calculated to be 3406.44 s^{-1} g^{-1} at 25 °C exposed to visible light, which was higher than in dark (red line κ = 2433.17 s^{-1} g^{-1}). When the samples were irradiated by light, the electron density decreases on the tip of the Au-Ag bimetallic satellite nanostructures, facilitating the adsorption of BH_4^- onto the surface of MS. The reduction action occurred via electrons transfer from the donor BH_4^- to the acceptor 4-NP on the tip of Au-Ag bimetallic. The hydrogen atom from the hydride, attacked 4-NP molecules to reduce it to 4-AP after the electron transfer to Au-Ag bimetallic.

3.3. In-situ SERS monitoring of catalytic reactions using $Fe_3O_4@TiO_2@Ag$-Au bimetallic MS

SERS provides non-destructive and non-invasive fingerprint characterization with widespread applications in biological and chemical sensing [46]. Compared to UV–vis spectroscopy, more exhaustive molecular-level information could be received by SERS. As reported the monometallic NPs loaded onto matrixes demonstrated to be SERS-active [47] while bimetallic NPs have been confirmed to be better than monometallic NPs [48,49]. In addition, the SERS signal can occasionally be affected by the affinity of an analyte functional group for the metal surface rather than

by the quantity of targets. In particular, metal has a strong affinity for thiol groups; thus, available target molecules for SERS detection are highly limited. So we choose 4-NTP as the model chemical to show that the $Fe_3O_4@TiO_2@Ag$-Au MS could be used in broader applications based on SERS based label-free detection. The $Fe_3O_4@TiO_2@Ag$ and $Fe_3O_4@TiO_2@Ag$-Au MS were dispersed in 4-NTP. Both MS exhibited unique 4-NTP SERS peaks at 1346 and 1590 cm^{-1}, respectively. This result indicates that $Fe_3O_4@TiO_2@Ag$-Au MS can be used as a SERS-based chemical detection tool. And in the comparative experiments, $Fe_3O_4@TiO_2@Ag$-Au MS with Au-Ag bimetallic satellite nanostructures can show the higher SERS signal enhancements.

Furthermore, the multifunctional $Fe_3O_4@TiO_2@Ag$-Au MS exhibited both outstanding SERS activity and highly efficient catalytic performances, which enables the in-situ SERS monitoring of surface catalytic reaction. The catalytic reduction of 4-NTP to 4-ATP by $NaBH_4$ is studied on $Fe_3O_4@TiO_2@Ag$-Au MS in view of the activity both in SERS and catalysis. To start this catalytic reaction, $Fe_3O_4@TiO_2@Ag$-Au MS was firstly immersed into 4-NTP aqueous solution, making $Fe_3O_4@TiO_2@Ag$-Au coated with adequate 4-NTP molecules, followed by the addition of $NaBH_4$ solution. To make the SERS signal intensity of the reaction system stable, $Fe_3O_4@TiO_2@Ag$-Au MS coated with 4-NTP was rearranged orderly with external magnetic field, the reaction continued smoothly for more hot spots existed and reserved during the course [50]. Fig. 4 demonstrates the SERS spectra of reaction solutions recorded
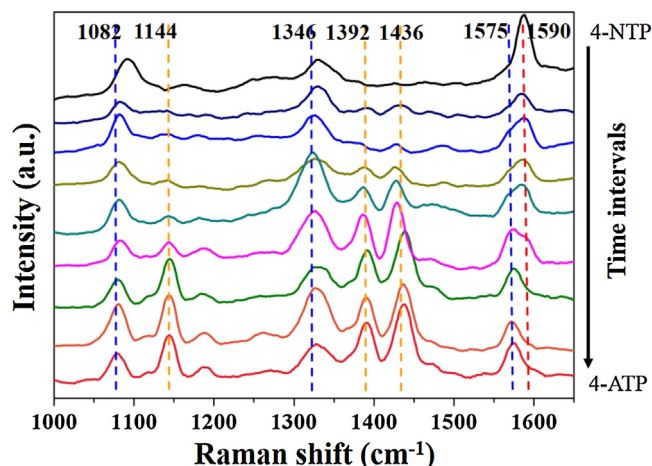
Fig. 4. SERS spectra recorded at selected time intervals after the addition of sodium borohydride to a 4-NTP-functionalized Fe$_3$O$_4$@TiO$_2$@Ag-Au MS surface under a magnetic field.

at 1 min intervals. The time-dependent spectra explained the characteristic bands of 4-NTP, such as the peak at 1346 cm^{-1} corresponding to ν(NO$_2$), and the two other peaks at 1082 cm^{-1} and 1590 cm^{-1} related to benzene ring vibrations. The peaks at 1144, 1392 and 1436 cm^{-1} appeared as soon as NaBH$_4$ was added, which was attributed to the spectral features of 4,4′-dimercaptoazobenzene (DMAB). As the reaction proceeded, DMAB was reduced to 4-ATP evidenced by the decrease in the intensity of 1144, 1392 and 1436 cm^{-1} bands and the appearance of new band at 1575 cm^{-1}, which correspond to 4-ATP, and the intensity increased with the increasing time. It can be proposed a serial hydride reduction of 4-NTP to DMAB and finally to 4-ATP [51]. As shown in Fig. S6, the nitro to amine reduction could be consid-

ered as a two-step consecutive reaction, either by a direct route by the hydroxylamine intermediate or by the condensation route (through the formation of an azo compound) [51]. In this work, it was shown that the 4-NTP to 4-ATP conversion could proceed through the dimerization and formation of DMAB when the reaction was catalysed by Au-Ag bimetallic satellite nanostructures.

3.4. Recovery ability of Fe$_3$O$_4$@TiO$_2$@Ag-Au MS

The potential recyclability of as-prepared Fe$_3$O$_4$@TiO$_2$@Ag-Au MS can be realized by the photocatalytic activity of TiO$_2$ under the visible light irradiation. As reported, metal NPs (Au or Ag) embedded in the matrix of TiO$_2$ make it more photocatalytically active [52–54]. The existence of Fe$_3$O$_4$ make it easy separate from the reaction medium within several seconds. The enhanced photocatalytical activity contributes to self-cleaning the molecules absorbed on it. The concentration changes of the 4-AP water solution versus irradiation time was shown in Fig. S7. Most of the photocatalytic reactions abide by the Langmuir-Hinshelwood (L-H) adsorption model [55], and the L-H model can be simplified to a pseudo-first-order expression: ln(C_t/C_0) = -kt (where C_0 and C_t are the initial and real-time concentration of 4-AP, and k is the linear plots of ln(C_t/C_0) versus irradiation time t) is attained and the photocatalytic reaction rate k of Fe$_3$O$_4$@TiO$_2$@Ag-Au is 0.1148 min^{-1} as shown in Fig. S7b. Thus, the Fe$_3$O$_4$@TiO$_2$@Ag-Au MS catalysts can realize the self-cleaning capability under visible light irradiation. And then the observed catalysts were washed with water and collected by magnet. Then the observed MS were dried for the catalytic reduction again. In Fig. S7c, the observed MS can be recycled and reused for at least 8 times with a stable conversion of ∼90%. The decrease of conversion after 8 cycles may be ascribed to the loss of nanocatalysts with the repeated magnetic separation.
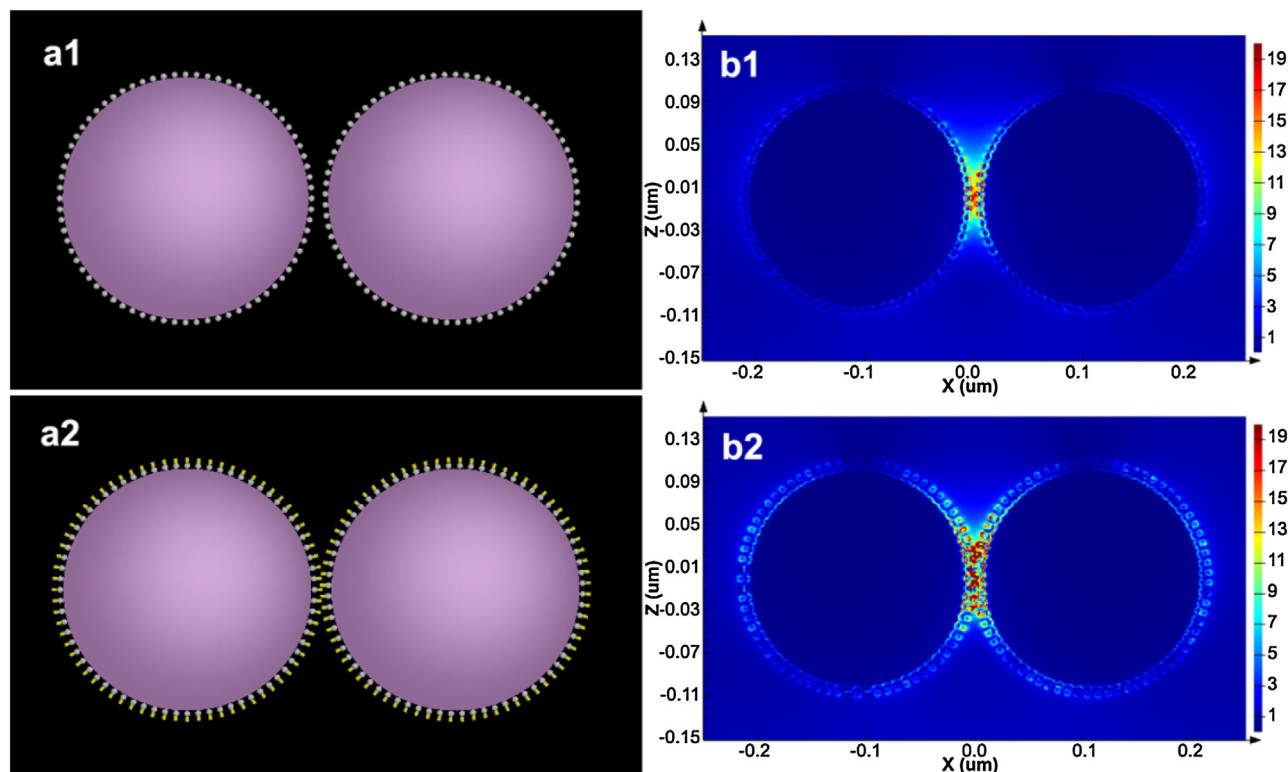
Fig. 5. The simulation model of Fe$_3$O$_4$@TiO$_2$@Ag (a1) and Fe$_3$O$_4$@TiO$_2$@Ag-Au (a2) and the electromagnetic field distributions of Fe$_3$O$_4$@TiO$_2$@Ag (b1) and Fe$_3$O$_4$@TiO$_2$@Ag-Au (b2). The incident light had a wavelength of 785 nm.

3.5. Simulation of Raman signal enhancement by Fe$_3$O$_4$@TiO$_2$@Ag-Au MS

To get insight into SERS enhancement of Fe$_3$O$_4$@TiO$_2$@Ag-Au MS, theoretical *E*-field distribution of Fe$_3$O$_4$@TiO$_2$@Ag (a1) and Fe$_3$O$_4$@TiO$_2$@Ag-Au (a2) was calculated by the discrete dipole approximation (DDA). The *E*-field distribution maps around the nanostructure and a plot of $(E/E_0)^2$ at the brightest spot on the incorporating Au nanopillars and Ag nanospheres bimetallic satellite nanostructureare shown in Fig. 5. As shown in the TEM images (Fig. 1), the measured SERS intensity of Fe$_3$O$_4$@TiO$_2$@Ag-Au was an ensemble average of enhanced Raman scattered light by the hot spots between the dimers of incorporating Au nanopillars and Ag nanospheres on Fe$_3$O$_4$@TiO$_2$ MS. In addition, the *E*-field intensity of the dimers increased compared to that of monomer due to the *E*-field concentration between noble nanostructures. Furthermore, the *E*-field intensity of the Fe$_3$O$_4$@TiO$_2$@Ag-Au MS dimers was the highest when the Au nanopillars were intertwined together. These results indicate that if the wavelength of incident light matches the localized surface plasmon resonance of the metal nanostructure, a strong localized electromagnetic field will be excited in the vicinity of the nanogaps [56], and there are hot spots between the nanoparticles gaps, which are agree with the experiments results. So this well design Fe$_3$O$_4$@TiO$_2$@Ag-Au MS with the incorporating Au nanopillars and Ag nanospheres bimetallic satellite nanostructures not only significantly increases the effect of the hot spots but also achieves stronger electromagnetic field enhancements between two microspheres compared to the Fe$_3$O$_4$@TiO$_2$@Ag MS. Finally, the prepared multifunctional Fe$_3$O$_4$@TiO$_2$@Ag-Au bimetallic MS also possess efficient catalytic activity during the repeated recycling process due to the outer layer of Ag-Au satellite nanostructures, which can be occurs electrons from Ag nanospheres to Au nanopillars to increase the reaction rate.

4. Conclusions

This work presents a controllable route towards the synthesis of Fe$_3$O$_4$@TiO$_2$@Ag-Au MS with different bimetallic molar ratio and shape. Ag-Au bimetallic structure assembled onto the Fe$_3$O$_4$@TiO$_2$@Ag-Au MS showed high catalytic activity for reduction of 4-NP to 4-AP as well as for 4-NTP to 4-ATP. The catalytic activity of composites is connected with factors including Au/Ag molar ratio and structures. The bimetallic catalysts exhibit excellent catalytic activity attached with in-situ SERS monitoring of reaction process, in addition, good photocatalytic performance make catalysts easy recovery for further use. Furthermore, FDTD simulation study displays that Fe$_3$O$_4$@TiO$_2$@Ag-Au MS significantly increases the effect of the 'hot spot', offering stronger electromagnetic field enhancements. So this work provides a new way to optimize catalysts with versatile functions.

Acknowledgments

Appendix A. Supplementary data

Supplementary data associated with this article can be found, in the online version, at http://dx.doi.org/10.1016/j.apcatb.2016.12.010.

References

[1] M.H. Huang, S. Mao, H. Feick, H.Q. Yan, Y.Y. Wu, H. Kind, E. Weber, R. Russo, P.D. Yang, Science 292 (2001) 1897–1899.
[2] Z.L. Wang, J.H. Song, Science 312 (2006) 242–246.
[3] J.H. Li, J.Z. Zhang, Coord. Chem. Rev. 253 (2009) 3015–3041.
[4] A. Villa, N. Dimitratos, C.E. Chan-Thaw, C. Hammond, G.M. Veith, D. Wang, M. Manzoli, L. Prati, G.J. Hutchings, Chem. Soc. Rev. 45 (2016) 4953–4994.
[5] J. Shen, Y. Zhu, X. Yang, C. Li, J. Mater. Chem. 22 (2012) 13341–13347.
[6] Y. Zhu, J. Shen, K. Zhou, C. Chen, X. Yang, C. Li, J. Phys. Chem. C 115 (2011) 1614–1619.
[7] C. Li, R. Younesi, Y. Cai, Y. Zhu, M. Ma, J. Zhu, Appl. Catal. B: Environ. 156–157 (2014) 314–322.
[8] P. Zhao, X. Feng, D. Huang, G. Yang, D. Astruc, Coord. Chem. Rev. 287 (2015) 114–136.
[9] S.E. Habas, H. Lee, V. Radmilovic, Nat. Mater. 6 (2007) 692–697.
[10] D. Xu, Z.P. Liu, H.Z. Yang, Q.S. Liu, J. Zhang, J.Y. Fang, S.Z. Zou, K. Sun, Angew. Chem. Int. Ed. 48 (2009) 4217–4221.
[11] S.Y. Song, R.X. Liu, Y. Zhang, J. Feng, D.P. Liu, Y. Xing, F.Y. Zhao, H.J. Zhang, Chem. Eur. J. 16 (2010) 6251–6256.
[12] S. Tang, S. Vongehr, X. Meng, J. Mater. Chem. 20 (2010) 5436–5445.
[13] J. Zeng, Q. Zhang, J. Chen, Y. Xia, Nano Lett. 10 (2010) 30–35.
[14] J. Wang, X.B. Zhang, Z.L. Wang, L.M. Wang, W. Xing, X. Liu, Nanoscale 4 (2012) 1549–1552.
[15] M.H. Rashid, R.R. Bhattacharjee, A. Kotal, T.K. Mandal, Langmuir 22 (2006) 7141–7143.
[16] W. Xie, B. Walkenfort, S. Schlücker, J. Am. Chem. Soc. 135 (2013) 1657–1660.
[17] E. Cortés, P.G. Etchegoin, E.C. LeRu, A. Fainstein, M.E. Vela, R.C. Salvarezza, J. Am. Chem. Soc. 132 (2010) 18034–18037.
[18] K.N. Heck, B.G. Janesko, G.E. Scuseria, N.J. Halas, M.S. Wong, J. Am. Chem. Soc. 130 (2008) 16592–16600.
[19] X. Li, M. Cao, H. Zhang, L. Zhou, S. Cheng, J.L. Yao, L.J. Fan, J. Colloid Interface Sci. 382 (2012) 28–35.
[20] L. Guerrini, E. Lopez-Tobar, J.V. Garcia-Ramos, C. Domingo, S. Sanchez-Cortes, Chem. Commun. 47 (2011) 3174–3176.
[21] J. Chao, W. Cao, S. Su, L. Weng, S. Song, C. Fan, L. Wang, J. Mater. Chem. B 4 (2016) 1757–1769.
[22] W. Xie, C. Herrmann, K. Kömpe, M. Haase, S. Schlücker, J. Am. Chem. Soc. 133 (2011) 19302–19305.
[23] W. Xie, B. Walkenfort, S. Schlücker, J. Am. Chem. Soc. 135 (2013) 1657–1660.
[24] M. Cao, L. Zhou, X. Xu, S. Cheng, J.L. Yao, L.J. Fan, J. Mater. Chem. A 1 (2013) 8942–8949.
[25] V. Joseph, C. Engelbrekt, J. Zhang, U. Gernert, J. Ulstrup, J. Kneipp, Angew. Chem. Int. Ed. 51 (2012) 7592–7596.
[26] F. Lin, R. Doong, J. Phys. Chem. C 115 (2011) 6591–6598.
[27] Z.Y. Bao, J. Dai, D.Y. Lei, Y. Wu, J. Appl. Phys. 114 (2013) 124305.
[28] W. Cai, X. Tang, B. Sun, L. Yang, Nanoscale 6 (2014) 7954–7958.
[29] X. Zhang, Y. Zhu, X. Yang, S. Wang, J. Shen, B. Lin, C. Li, Nanoscale 5 (2013) 3359–3366.
[30] J. Liu, Z. Sun, Y. Deng, Y. Zou, C. Li, X. Guo, L. Xiong, Y. Gao, F. Li, D. Zhao, Angew. Chem. Int. Ed. 121 (2009) 5989–5993.
[31] W. Li, J. Yang, Z. Wu, J. Wang, B. Li, S. Feng, Y. Deng, F. Zhang, D. Zhao, J. Am. Chem. Soc. 134 (2012) 11864–11867.
[32] Z. Qian, S.J. Park, Chem. Mater. 26 (2014) 6172–6177.
[33] Y. Qiu, Z. Ma, P.A. Hu, J. Mater. Chem. A 2 (2014) 13471–13478.
[34] K. Hayakawa, T. Yoshimura, K. Esumi, Langmuir 19 (2003) 5517–5521.
[35] S. Praharaj, S. Nath, S.K. Ghosh, S. Kundu, T. Pal, Langmuir 20 (2004) 9889–9892.
[36] J. Ge, Q. Zhang, T. Zhang, Y. Yin, Angew. Chem. 120 (2008) 9056–9060.
[37] J.M. Herrmann, Catal. Today 53 (1999) 115–129.
[38] K.S. Shin, Y.K. Cho, J.Y. Choi, K. Kim, Appl. Catal. A 413–414 (2012) 170–175.
[39] L. Xie, M. Chen, L.M. Wu, J. Polym. Sci. Part A: Polym. Chem. 47 (2009) 4919–4926.
[40] Z. Zhang, C. Shao, P. Zou, P. Zhang, M. Zhang, J. Mu, Z. Guo, X. Li, C. Wang, Y. Liu, Chem. Commun. 47 (2011) 3906–3908.
[41] K. Kuroda, T. Ishida, M. Haruta, J. Mol. Catal. A: Chem. 298 (2009) 7–11.
[42] R. Ferrando, J. Ellinek, R.L. Johnston, Chem. Rev. 108 (2008) 845–910.
[43] S. Tokonami, N. Morita, K. Takasaki, N. Toshima, J. Phys. Chem. C 114 (2010) 10336–10341.
[44] T. Wu, L. Zhang, J. Gao, Y. Liu, C. Gao, J. Yan, J. Mater. Chem. A 1 (2013) 7384–7390.
[45] Y. Zhu, Y. Zhu, X. Yang, J. Huang, W. Chen, X. Lv, C. Li, C. Li, RSC Adv. 5 (2015) 50454–50461.
[46] L. Li, T. Hutter, A.S. Finnemore, F.M. Huang, J.J. Baumberg, S.R. Elliott, U. Steiner, S. Mahajan, Nano Lett. 12 (2012) 4242–4246.
[47] X. Zhang, Y. Zhu, X. Yang, Y. Zhou, Y. Yao, C. Li, Nanoscale 6 (2014) 5971–5979.

[48] N.L. Netzer, C. Qiu, Y. Zhang, C. Lin, L. Zhang, H. Fong, C. Jiang, Chem. Commun. 47 (2011) 9606–9608.
[49] X. Li, M. Cao, H. Zhang, L. Zhou, S. Cheng, J.L. Yao, L.J. Fan, J. Colloid Interface Sci. 382 (2012) 28–35.
[50] W. Cai, X. Tang, B. Sun, L. Yang, Nanoscale 6 (2014) 7954–7958.
[51] G. Zheng, L. Polavarapu, L.M. Liz-Marzán, I. Pastoriza-Santos, J. Pérez-Juste, Chem. Commun. 51 (2015) 4572–4575.
[52] X.D. Wang, T. Dornon, M. Blackford, R.A. Caruso, J. Mater. Chem. 22 (2012) 11701–11710.
[53] O. Akhavan, E. Ghaderi, Surf. Coat. Technol. 204 (2010) 3676–3683.
[54] X. Wang, R.A. Caruso, J. Mater. Chem. 21 (2011) 20–28.
[55] J.M. Herrmann, Top. Catal. 34 (2005) 49–65.
[56] Z. Sun, J. Du, L. Yan, S. Chen, Z. Yang, C. Jing, ACS Appl. Mater. Interfaces 8 (2016) 3056–3062.